Journal of Oceanography (2023) 79:161–174
https://doi.org/10.1007/s10872-022-00673-2

ORIGINAL ARTICLE

The island mass effect: a study of wind-driven nutrient upwelling around reef islands

Jochen Kämpf[1] · Luciana Möller[1] · Ryan Baring[1] · Alex Shute[1] · Courtney Cheesman[1]

Received: 12 May 2022 / Revised: 20 November 2022 / Accepted: 23 November 2022 / Published online: 3 December 2022

Abstract

Using the method of process-oriented modelling, this study explores wind-driven upwelling features around reef islands of the tropical Pacific Ocean. The three-dimensional hydrodynamic model is coupled to a nutrient-phytoplankton (NP) model to simulate the creation of phytoplankton blooms initiated by the wind-driven upwelling of nutrients into the euphotic zone. Findings demonstrate that short-lived wind events of 2–5 days in duration, which are typical of tropical regions, can lead to significant phytoplankton blooms near reef islands. This finding agrees with observational evidence. Comparison studies reveal that the total phytoplankton production increases for higher wind speeds, longer durations of wind events and larger reef islands, and that it decreases with stronger static stability of the pycnocline. Overall, our findings indicate that wind-driven nutrient upwelling supports the ecosystem functioning around larger tropical reef islands.

Keywords Wind-driven upwelling · Tropical oceanography · Island mass effect · Reef islands · Subsurface phytoplankton blooms · Process-oriented modelling

1 Introduction

An island is a body of land surrounded by water. Geographically, the Pacific Ocean has most of the islands in the world. According to Nunn et al. (2016) the Pacific has 1779 islands with a surface area > 0.01 km^2, mainly located in tropical and subtropical regions. Most common are reef islands (36%) and volcanic high islands (31%). Recently, Messié et al. (2022) identified 11,449 islands and 4602 shallow reefs in the Pacific region from high-resolution bathymetry data; however, many of these islands form part of island groups that Nunn et al. (2016) counted as single islands. Reef islands include atolls that are circular or irregularly shaped, isolated oceanic reef structures at or near sea level that enclose a lagoon usually tens of meters deep (see Goldberg 2016). A key feature of atolls is the existence of steep reef fronts with slopes of up to 45°. Goldberg (2016) reported a global total of 439 atolls globally. The diameter of atolls ranges from 2.5 to nearly 100 km, but the mean value is about 20 km (Schwartz and King 2019). There is considerable variation in the geometry of reef crests around the perimeter of the central lagoon, ranging from continuous to highlight fractured. This study focusses on reef islands with a diameter < 40 km and steep reef fronts.

Groups of islands are often associated with enhanced plankton productivity due to various coupled physical-biogeochemical mechanisms, often summarized as "island mass effect" (Doty and Oguri 1956). These mechanisms include the interaction of oceanic flows with the island topography (Mann and Lazier 2005), tidal mixing around islands (Kodaira and Waseda 2019), tidally induced internal waves (Griffin et al. 1987), turbulent mixing in island wakes (Hasegawa et al. 2021), and other factors such as nutrient intake from island runoff (Bell 1992), atoll flushing (Gove et al. 2016), groundwater discharge (Hwang et al. 2005; Street et al. 2008) and human activities that increase nearshore nutrient concentrations above natural levels (Vitousek et al. 1997). It has also been demonstrated that wind-driven Ekman layers can create coastal upwelling on one side of an island and downwelling on the other side (Spall and Pedlosky 2013). In how much this wind-driven upwelling process can induce phytoplankton blooms around reef islands has not been systematically studied in the past.

✉ Jochen Kämpf
jochen.kaempf@flinders.edu.au
https://www.flinders.edu.au/people/jochen.kaempf

[1] College of Science and Engineering, Flinders University, Adelaide, Australia

The island mass effect is often inferred from satellite-derived chlorophyll-*a* (chl-*a*) levels as a proxy for surface phytoplankton concentrations. The surface chl-*a* signals near islands are generally 1–2 order of magnitude smaller than those characterizing major coastal upwelling systems (5–10 mg/m^3 in chl-*a*). For example, ship data around Madeira Island, Northeast Atlantic indicated maximum surface chl-*a* values of 0.15 mg/m^3 (Caldeira et al. 2002). Despite low surface levels, Messié et al. (2022) could identify surface chl-*a* enrichments near 99% of islands and submerged reefs of the tropical Pacific from satellite-derived data. On the other hand, phytoplankton biomass often increases deeper in the water column, reaching a subsurface maximum that can be far greater than in surface waters. For instance, Furuya (1990) detected enhanced chl-*a* levels of 0.3–0.4 mg/m^3 at a depth of ~ 100 m in the western Pacific. Findings by Gove et al. (2016) showed a significant increase of depth-integrated chl-*a* levels (dominated by subsurface signals) within 10 km from the coast from 25 in-situ surveys across 21 Pacific coral reef islands and atolls with values in a range of 1–10 mg/m^2.

There is indirect evidence of enhanced biological productivity near reef islands. For instance, a preliminary study on the fisheries catches in South China Sea using light falling nets (Wu et al. 2016) documented significant squid and tuna stocks around both the Paracel Islands and the Spratly Islands, which are regions of numerous atolls and shoals. With a net spanning an area of 3150 m^2 (equivalent to 63 m by 50 m), the average fishing rate was ~ 470 kg/h with purpleback flying squid (*Stenouteuthis oualaniensis*) comprising ~ 60% and yellowfin tuna (*Thunnus albacares*), skipjack tuna (*Katsuwonus pelamis*) and mackerel scads (*Decapterus maruadsi*) together comprising ~ 40% of the total catch. The "island mass effect" around the Paracel Islands and the Spratly Islands may explain why the South China Sea supports annual fish catches of the same order of magnitude as the world's most productive upwelling system off the coasts of Peru and Chile (Kämpf and Chapman 2016). Other indirect evidence comes from the feeding behaviour of baleen whales. For instance, pygmy blue whales (*Balaenoptera musculus brevicauda*) migrate from their feeding grounds located both near a coastal upwelling centre along the Bonney Coast (South Australia/Victoria, Australia) and the Perth Canyon (Western Australia) to Indonesian waters (Möller et al. 2020). Satellite tracks then show some whales near the Java coastal upwelling region and others near islands of the Inner Banda Arc—a volcanic arc of the Banda Sea (see Möller et al. 2020). Through wind-driven upwelling and other island-mass effects, these volcanic islands may provide a feeding ground for the whales.

The hypothesis of this work is that short-lived wind events induce localized upwelling near a reef island (Fig. 1a). This upwelling operates to lifts nutrient-enriched subsurface water into lower portions of the euphotic zone, where it triggers the creation of subsurface phytoplankton blooms. Strong upwelling or additional effects (e.g., enhanced vertical mixing) may trigger surface phytoplankton blooms. During and following a wind event, the zone of enriched nutrients and phytoplankton may spread away from the reef island under the effect of ambient currents over a distance that may exceed the island diameter (Fig. 1b).

Using the method of process-oriented hydrodynamic modelling, this work addresses the following scientific questions: (i) Are short-lived wind events with speeds of up to 10 m/s and durations of 3–6 days typical for tropical oceans? (ii) Can short-lived wind events near a reef island trigger the formation of substantial phytoplankton blooms? (iii) If so, which factors control the magnitude of this response?

2 Methodology

2.1 Conceptual model

Our model assumes that a transient wind event creates a surface Ekman layer of a volume transport of U_{ek} (m^2/s) that moves surface water away from the reef island (Fig. 2). The magnitude of the Ekman transport is given as follows:

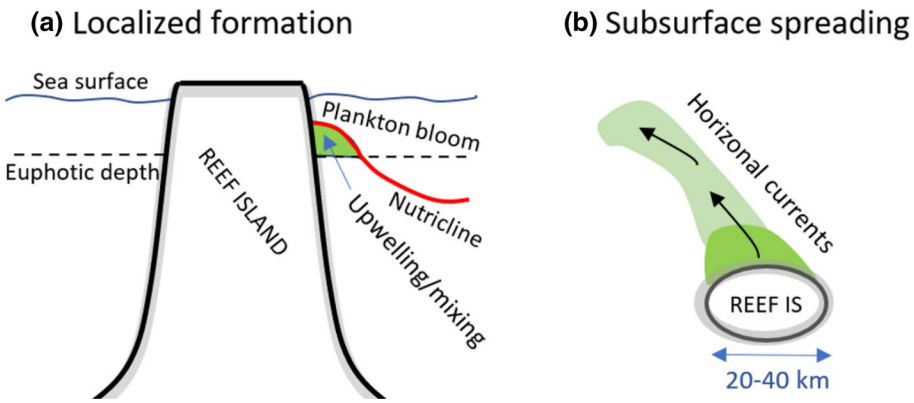

Fig. 1 Schematics of localized nutrient enrichment due to wind-driven upwelling. **a** Localized formation of a subsurface plankton layer near a reef island. **b** Its subsequent spreading under the effect of ambient currents over horizontal distances that may exceed the island size

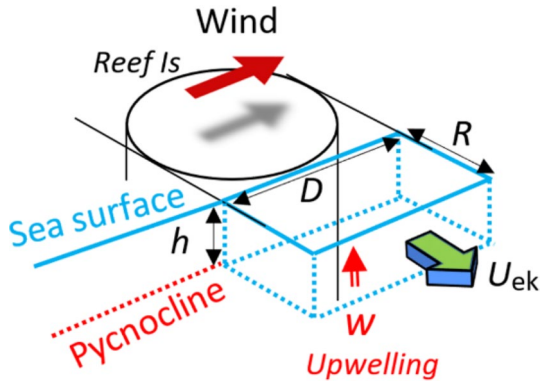

Fig. 2 Schematic illustrating the wind-driven upwelling process around a reef island of diameter D. The wind event creates an offshore Ekman volume transport U_{ek} that is balanced by an upward volume transport over a distance R associated with a vertical upwelling velocity W

$$U_{ek} = \frac{|\tau|}{(\rho_o |f|)}, \tag{1}$$

where τ is wind stress, $\rho_o \approx 1026$ kg/m^3 is an average seawater density, and f is the Coriolis parameter. This assumption is not valid in close vicinity (< 100 km) of the equator where the Coriolis force vanishes, and it may not fully apply on timescales shorter than the inertial period, which is ~ 36 h at a geographical latitude of 20°N. Ekman transport is perpendicular to the wind direction. Next, we assume that this Ekman transport is fully balanced by upwelling of subsurface water rather than by horizontal inflows. Based on volume conservation, the average upwelling speed W is then given as follows:

$$W = U_{ek}/R = \frac{|\tau|}{(\rho_o f R)}, \tag{2}$$

where R is the width of the upwelling zone. Over the duration of a wind event, t_w, this vertical speed operates to lift the nutricline upward by a distance of the following:

$$\Delta h = t_w W = t_w |\tau| / (\rho_o f R) \tag{3}$$

For an ocean with a flat, deep bottom, R can be represented by the internal Rossby radius of deformation (Cushman-Roisin and Beckers 2011). For a two-layer ocean with a thin surface layer of thickness h and density anomaly $\Delta\rho$, the internal deformation radius is given by $R = \sqrt{g' h}/f$ with $g' = \Delta\rho/\rho_o\, g$ where g is acceleration due to gravity, and we yield the following:

$$\Delta h = t_w |\tau| / \left(\rho_o \sqrt{g' h}\right) \tag{4}$$

Given that Δh and R are inversely related to each other, increased density stratification operates to reduce the vertical displacement while widening the upwelling zone. Let us consider the example of a reef island with a diameter of $D = 20$ km located at a geographical latitude of 20°N corresponding to $f = +0.5 \times 10^{-4}$ s^{-1}. Assume a surface mixed layer with $h = 50$ m and $\Delta\rho = 1$ kg/m^3, corresponding to $R = 13.8$ km. According to Eq. (4), a wind event of $\tau = 0.054$ Pa (wind speed is 6 m/s) lasting for $t_W = 4$ days induces a vertical displacement of $\Delta h \approx 26$ m that can lift nutrient-enriched water into the euphotic zone.

Based on the above, we expect that both the vertical displacement (Δh) and the horizontal extent of the upwelling zone (D) are primary physical controls of the initial amount of phytoplankton biomass produced by the wind-driven upwelling process. Accordingly, we expect that the latter increases for (i) longer and stronger wind events and (ii) larger islands, and that it decreases for enhanced static stability of the water column.

2.2 Model description

2.2.1 Overview

This study applies a fully coupled simplified physical-biological model to predict nutrient upwelling and phytoplankton production around a reef island under the action of a short-lived wind event (2–5 days in duration) over a timescale of two weeks. For simplicity, additional effects due to zooplankton grazing and nutrient-recycling by bacteria are ignored. The biological model is used as diagnostic tool to derive the amount of nitrate available for photosynthesis and the production rate of phytoplankton for the comparison of different model scenarios.

2.2.2 Physical model

This study applies the hydrodynamic model COHERENS (Luyten et al. 1999). The governing equations are the finite-difference forms of conservation equations for momentum, heat, volume and scalars (salinity) for an incompressible fluid on the f plane cast in terrain-following sigma coordinates. COHERENS is based on the same physical laws and coordinate transformation and similar numerical algorithms that govern other sigma coordinate models such as POM (Blumberg and Mellor 2013) or ROMS (Shchepetkin and McWilliams 2005). The Coriolis parameter is set to $f = +0.5 \times 10^{-4}$ s^{-1}, corresponding to a geographical latitude of 20°N. Variations of f yielded similar results (not shown). Horizontal turbulence is parameterized using the closure scheme by Smagorinsky (1963). Vertical turbulence is parameterized with the k-ε turbulence closure using standard parameter settings (see Luyten et al. 1999). The use of the level 2.5 closure of Mellor and Yamada (1982) with the modifications introduced by Galperin et al. (1988) yielded

qualitatively similar results (not shown). Eddy viscosities are assumed to be the same magnitude as eddy diffusivities. Bottom friction is disabled. Variations of turbulence parameters had no significant influence on the results. Under the assumption of a linear equation of state and ignoring double-diffusive processes, density anomalies are predicted from an advection–diffusion equation that, which the same eddy diffusivities, is also used to predict changes in phytoplankton and nitrate concentrations.

2.2.3 Biological model

The biological model is directly coupled with the physical model sharing the same numerical grid and time step. It is derived from a Nitrogen-Phytoplankton (NP) model adopted from the Nitrogen-Phytoplankton-Zooplankton-Detritus (NPZD) model described by Ji et al. (2007). The NP model focusses exclusively on the initial growth rate of phytoplankton based on the combination of photosynthetically available radiation (PAR) and nutrient levels. The conservation equations for dissolved nitrogen concentration (N) and phytoplankton concentration (P) are given by the following:

$$\partial N/\partial t + \mathrm{Adv}(N) = \mathrm{Diff}(N) - \mu P, \tag{5}$$

$$\partial P/\partial t + \mathrm{Adv}(P) = \mathrm{Diff}(P) + (\mu - \lambda)P, \tag{6}$$

where t is time, Adv(.) and Diff(.) are three-dimensional advection and diffusion operators, μ is the in-situ phytoplankton growth rate and μ is the phytoplankton mortality rate.

The NP model is driven by photosynthetically available radiation, I, that is approximated by the classical exponential light-attenuation curve:

$$I(t,z) = I_o(t)e^{-a_w z}, \tag{7}$$

where I_o is surface radiance, z is depth and a_w is light attenuation coefficient, set to $a_w = 0.1\ \mathrm{m}^{-1}$. Effects due to self-shading by particles are ignored here. Surface radiance varies as function of the day–night sunlight cycle which is taken as:

$$I_o(t) = \max\left[I_{oo}\sin(2\pi t/T), 0\right], \tag{8}$$

where I_{oo} is set to 500 W m^{-2}, t is time, and T is the duration of a day. The magnitude of I_{oo} is based on PAR measurements in the tropical zone of the South China Sea (Hanelt 1992). The phytoplankton growth rate (μ), which appears as a decay parameter in the nitrogen Eq. (5), can then by formulated by (e.g., Ji et al. 2007):

$$\mu = \mu_* \frac{N}{(K_N + N)} \text{ with } \mu_* = \mu_{\max}\left(1 - e^{-\hat{\alpha}I}\right)e^{-\hat{\beta}I}, \tag{9}$$

where $\mu_{\max}$ is largest possible phytoplankton growth rate under both saturated light and nutrient conditions, N is the *in-situ* nitrogen concentration, K_N is the half saturation constant of phytoplankton uptake of nitrogen, taken as $K_N = 1.0$ µM-N, $\hat{\alpha} = 0.025\ (\mathrm{Wm}^{-2})^{-1}$ is the initial slope of the P-I curve normalized to $\mu_{\max}$, $\hat{\beta} = 0.001\ (\mathrm{Wm}^{-2})^{-1}$ is the light inhibition coefficient, and I is the photosynthetically available radiation (PAR). Furnas (1990) reported measured or estimated growth rates of phytoplankton assemblages for tropical and subtropical oceans in a large range from 0.1 to 2.5 day^{-1}. Based on this range, this study uses values of $\mu_{\max} = 1.5$ day^{-1} in conjunction with a mortality rate of $\lambda = 0.05$ day^{-1}. Equation (9) includes the effect of photoinhibition of photosynthesis of marine phytoplankton, first derived by Platt et al. (1980).

The daily average of μ_*, denoted as $\langle \mu^* \rangle$, peaks at ~ 0.55 day^{-1} at a depth of 10 m (Fig. 3a). Net phytoplankton growth is impossible below a depth of 47 m, where $\langle \mu \rangle_* < \lambda$ irrespective of nutrient levels. On the other hand, from the condition $\langle \mu \rangle > \lambda$, we can infer minimum nitrogen values required to support net phytoplankton growth at shallower depths from the following relation:

$$N_{\min} = \begin{cases} \frac{K_N \lambda}{(\langle \mu_* \rangle - \lambda)} & \text{for } \langle \mu_* \rangle > \lambda \\ \infty \text{ otherwise} \end{cases} \tag{10}$$

Figure 3b shows the vertical profile of $N_{\min}$ for the configuration of this study. In the following, we define the photosynthetically available nitrogen (PAN) as follows:

$$\mathrm{PAN} = \max(N - N_{\min}, 0) \tag{11}$$

Chlorophyll-a levels are calculated on the basis of an average C:chl-a ratio of 50:1 (see Jakobsen and Markager 2016) and a Redfield ratio of C:N of 106:16. This yields a conversion ratio between phytoplankton in units of µM-N and chlorophyll-a in units of mg/m^3 of 1:1.59. All experiments assume a small initially uniform ambient chl-a concentration of 0.1 mg/m^3.

2.3 Experimental design

The model bathymetry of the control experiment is a simplified circular reef island, 20 km in diameter (Fig. 4). It is cast in a model domain of 80 km by 80 km in horizontal extent, resolved by a horizontal grid spacing of $\Delta x = \Delta y = 500$ m. On this horizontal resolution, the reef island is represented in the physical model as a vertical cylinder. Strong static stability of the pycnocline below a depth of 50 m suppresses the creation of deeper flows. This feature allows us to limit the maximum water depth to 100 m, which significantly reduces the CPU time of model simulations. Test studies doubling the maximum depth gave similar results (not shown). The

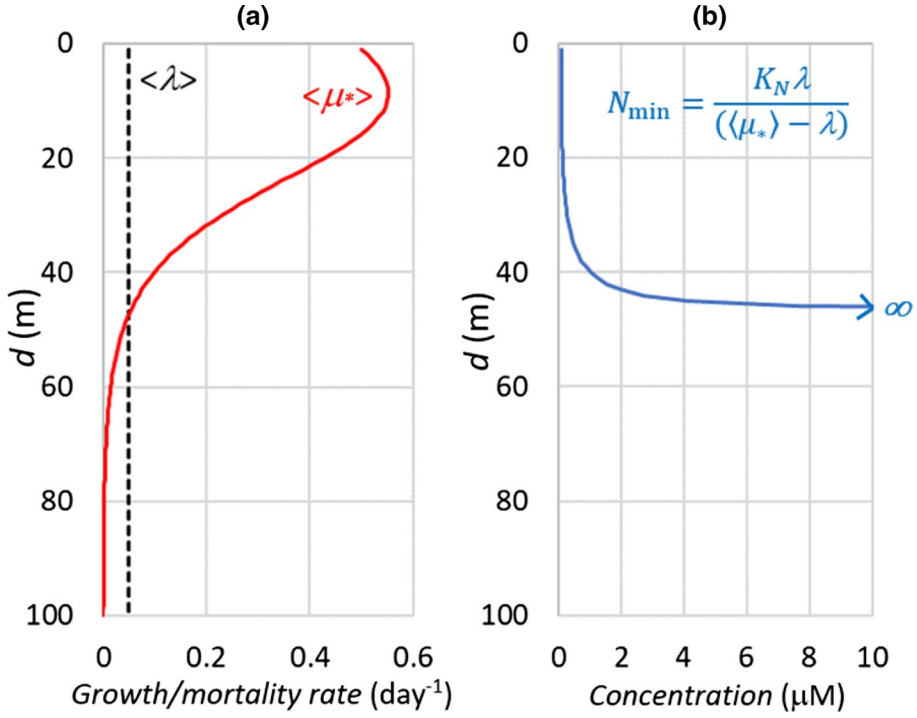

Fig. 3 Vertical profiles of **a** daily averaged value ⟨.⟩ of the largest possible phytoplankton growth rate under saturated nutrient conditions, μ_* (day^{-1}), for the configuration of this study. The dashed line displays the mortality rate; **b** the minimum nitrogen concentration N_{min} (μM) required to induce phytoplankton growth in the euphotic zone

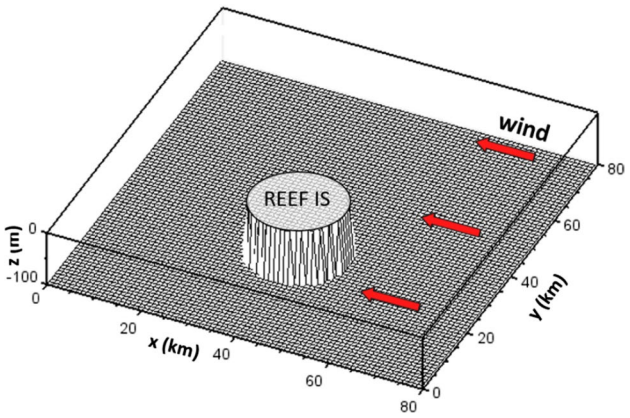

Fig. 4 Model bathymetry considered in the control experiment of this study. Arrows indicate the wind direction

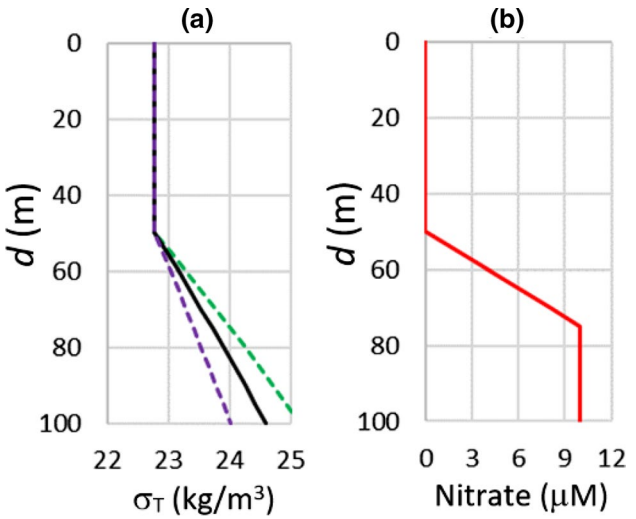

Fig. 5 Model configuration. Initial vertical profiles of **a** seawater density excess (σ_T; kg/m^3) relative to 1000 kg/m^3 (the black line shows the configuration of the control experiment; dashed lines show variations), and **b** nitrogen as dissolved nitrate concentration (μM)

vertical extent of the water column is resolved by 20 sigma layers, yielding a vertical grid spacing of 5 m. The island diameter is varied between 10 and 40 km in comparison studies.

The initial ocean's density field is represented by a 50 m-thick surface mixed layer followed by a stably stratified pycnocline characterized by a linear density increase (Fig. 5a). The surface mixed layer is initially devoid of nitrogen. Dissolved nitrate concentration increases below the surface mixed layer linearly to a maximum of 10 μM at a depth of 75 m, with constant values underneath (Fig. 5b). This setting remains unchanged in all simulations. The static stability of the pycnocline is based on field observations from the tropics (Sprintall and Tomczak 1992). The pycnocline in the control experiment has a stability frequency of $M = 0.0183$ s^{-1} (defined by $M^2 = -g/\rho_o d\rho/dz$) corresponding to a density increase of 1.83 kg/m^3 over the 50-m thickness of the pycnocline. The stability frequency is varied in comparison studies between $M = 0.0155$ s^{-1} and 0.0214 s^{-1}, corresponding to density increases ranging from 1.25 to

Table 1 List of experiments

Experiment	W (m/s)[a]	D (km)[b]	t_w (days)[c]	M (s^{-1})[d]
Control	10	20	4	0.018
1a,b,c,d	10	20	1, 2, 3, 5	0.018
2a,b,c,d	6, 7, 8, 9	20	4	0.018
3a,b,c	10	10, 30, 40	4	0.018
4a,b	10	20	4	0.015, 0.021

[a]Wind speed

[b]Island diameter

[c]Duration of wind event

[d]Stability frequency of pyncocline

2.4 kg/m^3 over the 50-m thickness of the pycnocline. For simplicity, the effect of barrier layers (see Sprintall and Tomczak 1992, Cronin and McPhaden 2002) is not considered in this study.

All simulations begin with a state at rest; that is, ambient currents are ignored in this study. All experiments are forced by a uniform easterly wind, blowing antiparallel to the x-direction. Results are independent of the wind direction. The wind speed is linearly increased from zero to a constant value over the first simulation day to avoid the generation of unwanted gravity waves. The wind forcing is turned off after a certain duration t_w. Wind speeds and durations of wind events are varied in comparison studies in a range of 6–10 m/s and 1–5 days, respectively, based on the analysis of wind data presented in Sect. 3.1. Wind stress components are calculated from wind velocity using standard quadratic bulk formulae with a wind drag coefficient of $c_D = 0.0012$. Zero-gradient conditions are used at all horizontal boundaries. In addition, Rayleigh damping is applied to sea level anomalies within 5 km from lateral boundaries with a damping coefficient that linearly increases to a maximum value of 0.1 at the boundaries. The coupled physical-biological model is run with a time step of $\Delta t = 7.8$ s (constrained by stability criteria) over a total of 14 days with daily data outputs.

Experiments comprise 14 different scenarios considering variations of wind speed (W), the diameter of the circular reef island (D), the duration of wind events (t_w) and the stability frequency of the pycnocline (M) (Table 1).

2.4 Analysis

Apart from analysing surface distributions of all variables, we also calculate vertically integrated chlorophyll-a concentrations (mg/m^2), the total amount of chlorophyll-a (kg) produced and total phytoplankton production rates Φ (kg/day). In addition, the total amount of photosynthetically available nitrogen (PAN) is calculated using Eq. (11). Vertical nitrate fluxes are derived from temporal changes of PAN and the estimated area of the upwelling zone. To avoid biases arising from the integration of small values over a large volume, these calculations ignore grid elements where phytoplankton concentrations are at or below the initial value.

3 Results and discussion

3.1 Wind variability in selected tropical regions

To understand the characteristic timescale of wind events in tropical marine regions associated with tropical storms, we selected four locations in the western Pacific Ocean, including one location in the South China Sea (~ 11°N, 115.4°E) and three locations at ~ 140°E in the Philippine

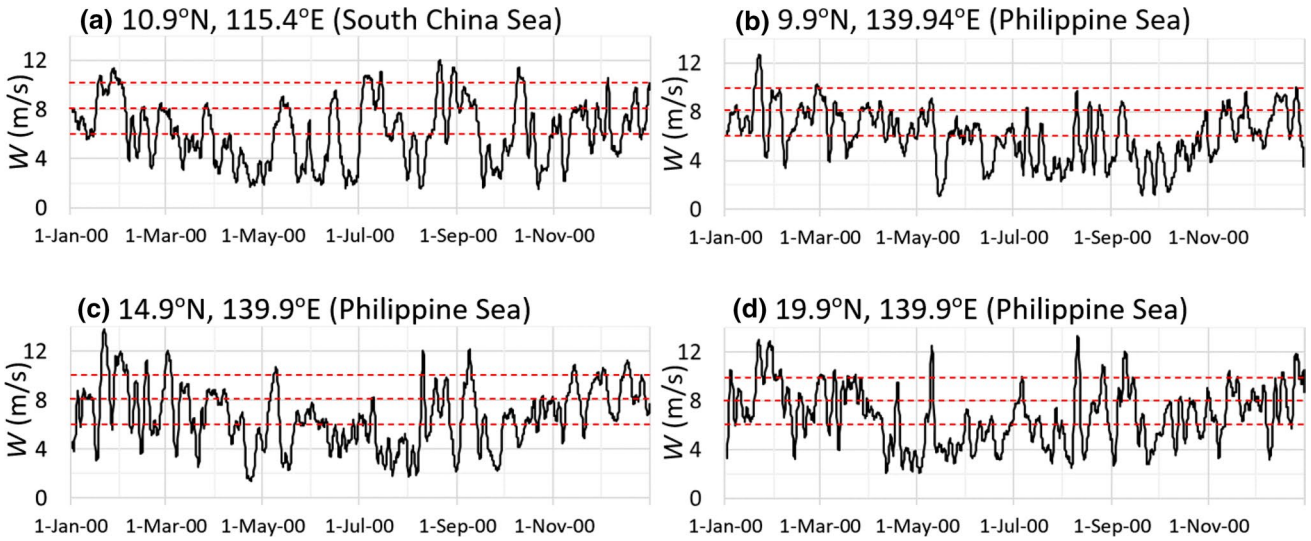

Fig. 6 Time series of daily wind speed W (m/s) at selected locations in the western Pacific Ocean for the year 2000. Data: Ifremer 6-hourly Long Time Series Satellite Surface Wind Analyses, available at http://apdrc.soest.hawaii.edu/data/data.php. Wind speeds of 6, 8 and 10 m/s are marked by dashed red lines

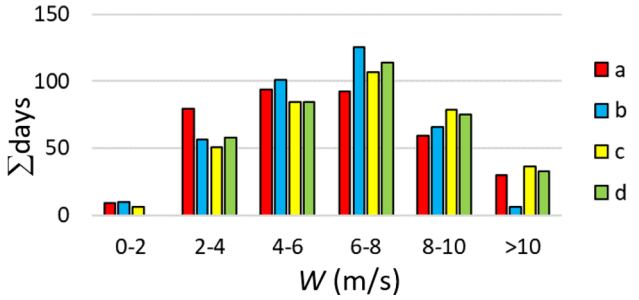

Fig. 7 Histogram of wind data shown in the panels **a**–**d** of Fig. 6

Sea at geographical latitudes of ~ 10°N, ~ 15°N and ~ 20°N. Figure 6 shows daily wind speed data (at 10 m above sea level) for the year 2000 for these locations. The wind variability for other years is statistically similar (not shown).

The histogram of the wind data reveals that wind speeds in the range 6–8 m/s are most common in these regions occurring on ~ 100 days per year (Fig. 7). Stronger winds > 8 m/s occur on ~ 50 days per year. A detailed event analysis shows that all regions experience a large number (> 8) of prolonged periods (> 7 days) of lower wind speeds around 6 m/s (Fig. 8). However, stronger wind events are rarer. In the South China Sea, for instance, we can identify a total of 7 wind events exceeding a speed of 10 m/s and lasting between 2 and 8 days (Fig. 8a). Figure 7a shows the timing of these events, some of which occur shortly after each other. Strong wind bursts of $W > 10$ m/s are rarer at 10°N in the Philippine Sea compared with the other locations, but there are still relatively strong wind events (8–10 m/s speed) lasting up to a week. In summary, the event analysis for the regions confirms that stronger wind events of durations between 1 and 7 days are a common feature of the tropical Pacific. While the wind direction can vary by > 90° during a wind event, there are many instances during which the wind direction remains relatively steady (Fig. 9). This justifies the use of a constant wind direction in the model simulations.

3.2 Control experiment

The wind forcing creates a surface Ekman layer characterized by northwestward surface currents (which are characteristic of the classical Ekman spiral) within the first couple of simulation days (Fig. 10). In interaction with the island, the Ekman drift creates zones of horizontal flow divergence or convergence that are reflected in sea-surface anomalies. Analogous to the wind-driven coastal upwelling/downwelling process, negative sea level anomalies (of up to − 0.4 cm here) are aligned with the upwelling zone and positive anomalies mark the downwelling zone (see Spall and

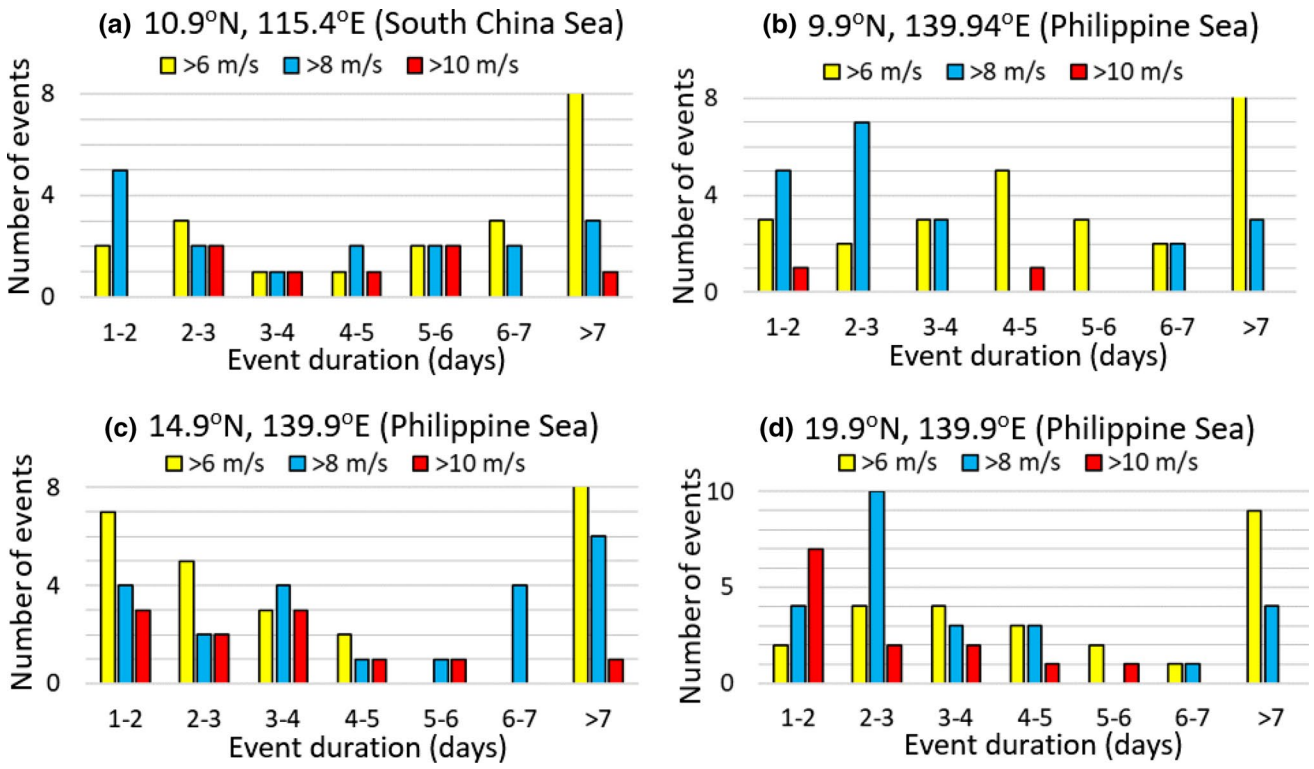

Fig. 8 Event analysis of the wind data shown in Fig. 7, displaying the number of continuous events (*y*-axis) of a certain duration (*x*-axis) that exceed a certain threshold wind speed (legend). Events < 1 day are not shown

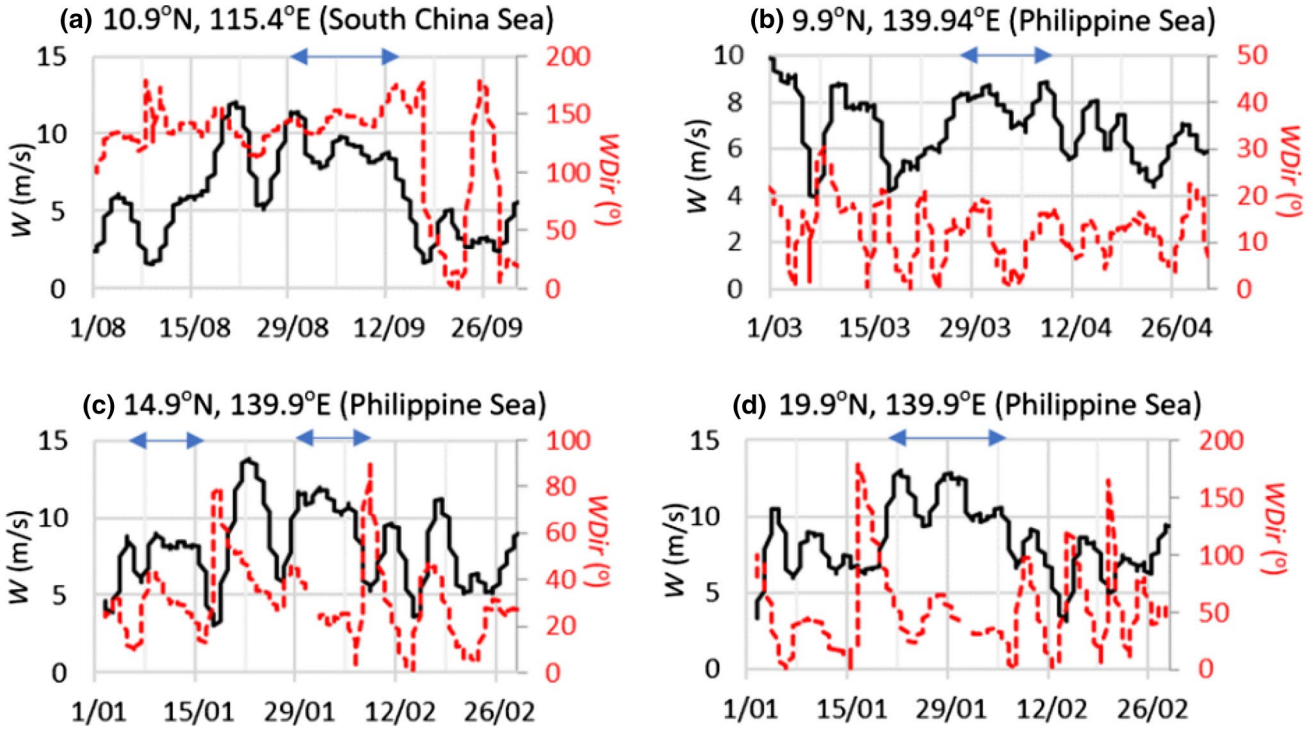

Fig. 9 Selected 2 months periods of the year 2000 displaying variations of wind speed, *W*(m/s), and wind direction, *Wdir* (°). Wind direction is based on the meteorologic convention that northerlies (easterlies) correspond to a direction of 0° (90°). Arrows indicate wind events that display little (< ± 20°) variation of the wind direction

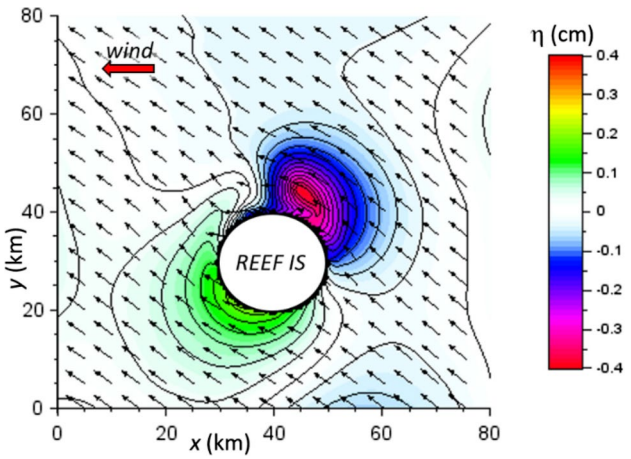

Fig. 10 Control experiment. Sea-level anomalies, η (cm) (thin lines and color shading), and currents in the surface layer (arrows, every 10th vector is shown) after 4 days of simulation. Maximum current speed is 0.15 m/s

Pedlosky 2013). Due to geostrophic adjustment, the associated horizontal pressure-gradient force leads to deflections of surface currents near the reef island.

The horizontal structure of the wind-driven upwelling zone becomes obvious from the development of the surface distributions of dissolved nitrogen. These increase to concentrations > 1 μM within the upwelling zone during the period of wind forcing (Fig. 11a). The zone of nutrient enrichment forms on the northern side of the reef island oriented perpendicular to the wind direction, which is consistent with Ekman theory underpinning our conceptual model (see Sect. 2.1). After 3 days of simulation, the zone of nutrient enrichment extents an area of approximately 400 km^2.

After cessation of the wind forcing, the upwelling zone becomes deformed under the continued action of ambient currents, and it develops two distinct features (Fig. 11b–d). One feature is the spreading of the coastal signal clockwise around the reef island in form of Kelvin waves. After 12 days of simulation, seawater with elevated nitrate concentrations > 0.3 μM surrounds the entire island within ~ 5 km from the coast. The other feature is a stationary cyclonic eddy, ~ 8 km in diameter, forming at a distance ~ 10 km from the east coast of the reef island, trapping nutrient-enriched seawater in its centre.

Under the effects of vertical turbulence, the upwelled nitrogen becomes vertically evenly distributed throughout the surface mixed layer (Fig. 12). This differs from our conceptual model (see Sect. 2.1) that does not account for mixing effects. The strong static stability of the pycnocline counteracts the upwelling process such that the level of upwelled nitrogen in the surface mixed layer remains relatively low (~ 1 μM). Nevertheless, this nitrogen anomaly

exceeds the minimum value (see Fig. 3b) and hence is sufficient to induce phytoplankton growth. To this end, the wind-driven nutrient upwelling process facilitates the production of phytoplankton in the upwelling zones of nutrient enrichment (Fig. 13). After two weeks of simulation, chlorophyll-*a* concentrations attain vertically integrated values of up to 10 mg/m^2 and surface values of up to 0.2 mg/m^3 in the offshore eddy and in a 10-km wide near-coastal patch. Note that the region of peak phytoplankton production is eventually located on the upwind side of the island.

The coastal upwelling process leads to sharp increase of photosynthetically available nitrogen (PAN) in the euphotic zone (Fig. 14b). The total amount of PAN increases from zero to ~ 4.5×10^6 kg between days 2 and 4 of the simulation. Based on an estimated upwelling area of 400 km^2, this change in PAN corresponds to a vertical nitrate flux of ~ 500 mmol/m^2/day (Fig. 14c), which is within the order of values (1–1000 mmol/m^2/day) reported for a turbulent island wake (Hasegawa et al. 2021). After cessation of the wind forcing, the total amount of PAN remains relatively constant (see Fig. 14b), which implies a significant drop in vertical nutrient fluxes (see Fig. 14c). The upwelling-induced nutrient-enrichment triggers a steady increase in phytoplankton biomass that commences after 3 days of simulation and results in the production of ~ 1060 kg of chlorophyll-a after 14 days of simulation (Fig. 14a). By this time,

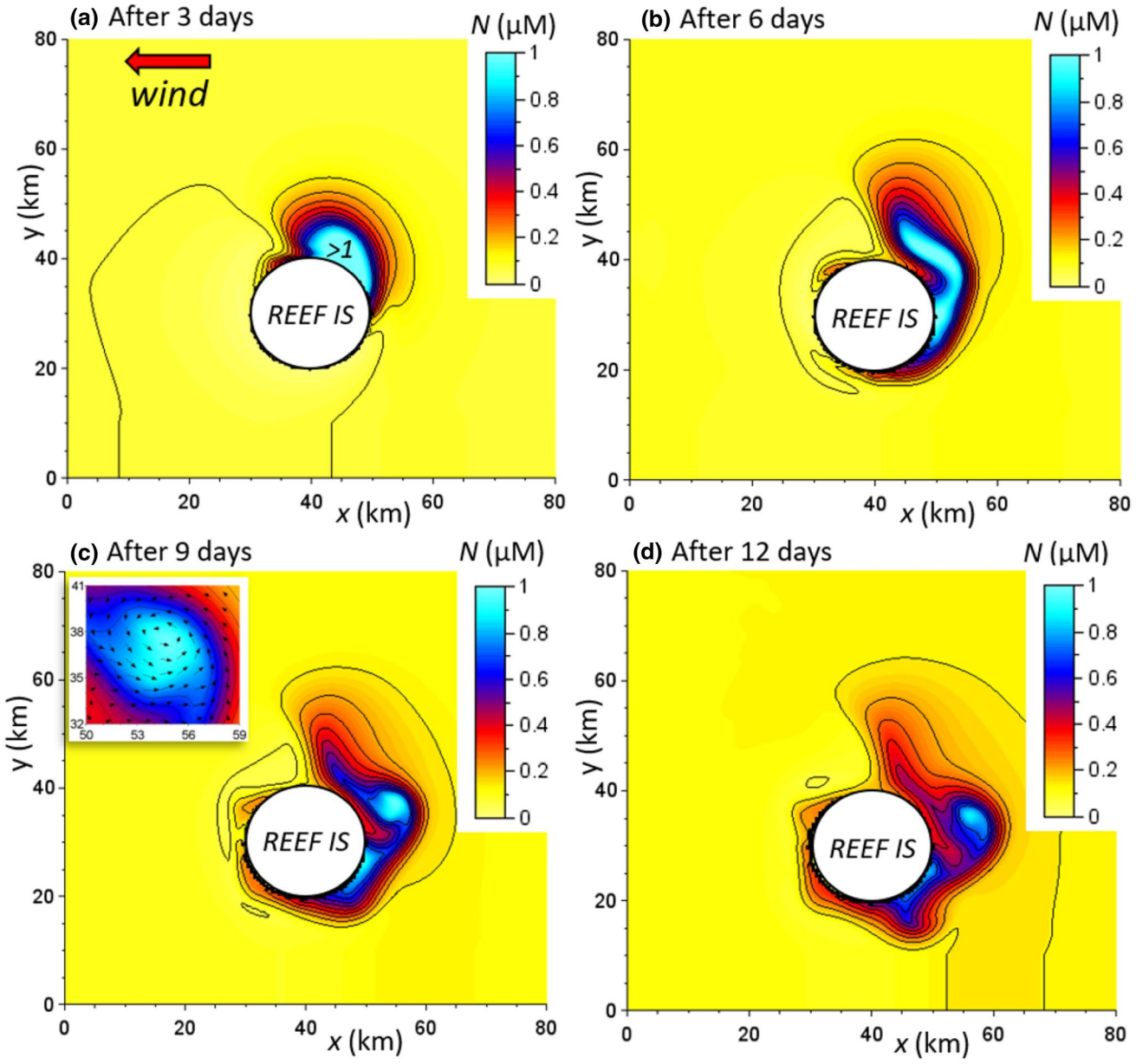

Fig. 11 Control experiment. Surface distributions of nitrogen concentrations, *N* (μM), after **a** 3 days, **b** 6 days, **c** 9 days, and **d** 12 days of simulation. The insert in (**c**) shows horizontal currents around the cyclonic eddy (arrows, every 2nd vector is shown)

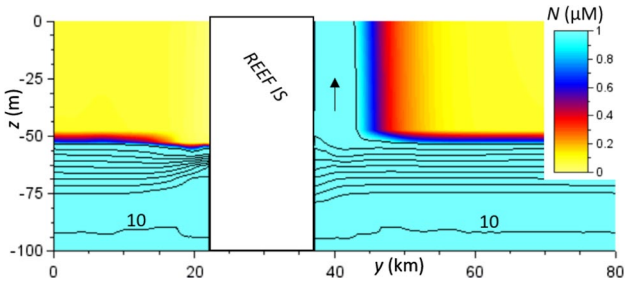

Fig. 12 Control experiment after 3 days of simulation. Vertical transects at $x_o = 47$ km (see Fig. 11) of dissolved nitrogen concentration, N (μM). Colour shading shows concentrations up to 1 μM. Lines are contours with an interval of 1 μM

the nitrate loss due to photosynthesis amounts to ~ 45 mmol/m^2/day (see Fig. 14c), which is still too small to influence PAN concentrations in the euphotic zone.

3.3 Variation experiments

In the following the change in total chlorophyll-*a* biomass over the second simulation week is taken as a measure of the average phytoplankton production rate Φ (kg/day) to compare different model scenarios. Overall, the derived value of Φ is strongly correlated to the total amount of PAN created during the upwelling period (Fig. 15). Hence, there is a strong relationship between the initial vertical nitrate flux during the upwelling phase and the phytoplankton production that follows from it. Accordingly, Φ and PAN are interchangeable properties in the following analysis.

The duration of wind events, t_w, has a strong effect on the phytoplankton biomass produced from the nutrient upwelling (Fig. 16a). A wind duration of a day does not induce a phytoplankton response in the control experiment. Once this threshold is exceeded, the phytoplankton production rate Φ increases linearly with t_w, which is consistent with Eq. (3) of our conceptual model. Hence, a longer wind event triggers a larger vertical displacement of the nutricline, which leads to increased nutrient levels and increased phytoplankton grow rates. The delay time of a day is caused by several factors. First, due to linear adjustment, the wind field is weaker during the first simulation day. Second, it takes several hours of simulation for surface Ekman layers to become stationary in response to the uniform wind forcing. Third, there is a delay in the time it takes for the initial nutricline located at depths > 50 m (see Fig. 5b) to reach the euphotic zone of enhanced growth rate at depths < 40 m (see Fig. 3a).

The magnitude of the wind stress, τ, has also a strong effect on Φ (Fig. 16b). With a duration of 4 days, a relatively weak wind of 6 m/s, corresponding to a wind stress of $\tau \approx 0.05$ Pa, only results in a small value of $\Phi \approx 4.3$ kg/day, whereas a 10-m/s wind ($\tau \approx 0.15$ Pa) triggers a substantial increase in production rates to $\Phi \approx 100$ kg/day. Note that phytoplankton blooms do not develop for winds weaker than 0.05 Pa where reduced upwelling speeds fail to move nutrient-enriched water into the euphotic zone within the given time limit. Again, this is related to the choice of initial conditions, and it is not an indicator of a nonlinear relationship between Φ and τ. If we ignore this delay feature, the relationship between τ and Φ can be approximated by a linear function, which is consistent with Eq. (3).

The diameter of the reef island, D, also strongly influences the phytoplankton production rate Φ with an approximately linear relationship (Fig. 16c). A small island with a diameter of 10 km produces only little phytoplankton biomass, whereas larger reef islands with a diameter of 40 km

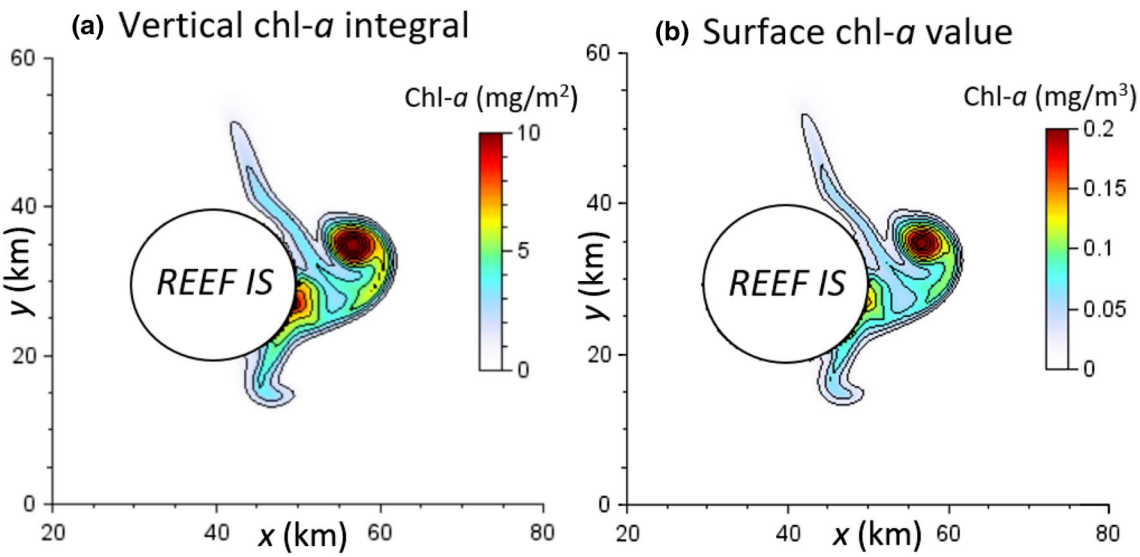

Fig. 13 Control experiment. Vertically integrated chlorophyll-*a* concentration (mg/m^2) after 14 days of simulation

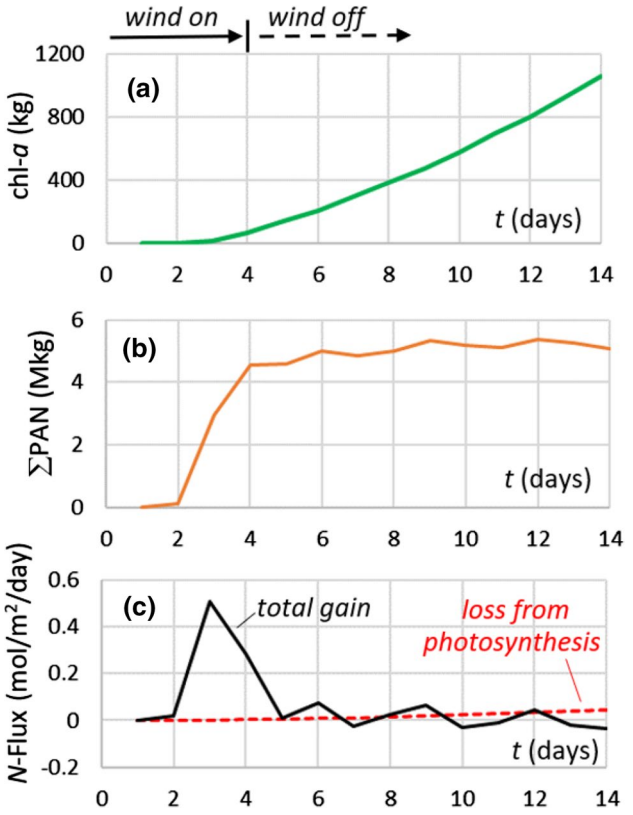

Fig. 14 Time series of **a** total amount (kg) of chl-*a* produced, **b** total amount of photosynthetically available nitrogen (PAN, 10^6 kg) created by oceanic processes, and **c** (black line) the nutrient flux (mol/m^2/day) based on the values shown in (**b**) and an estimated upwelling area of 400 km^2 in size. The dashed red line shows the nitrate loss from photosynthesis calculated from the last term in Eq. (5)

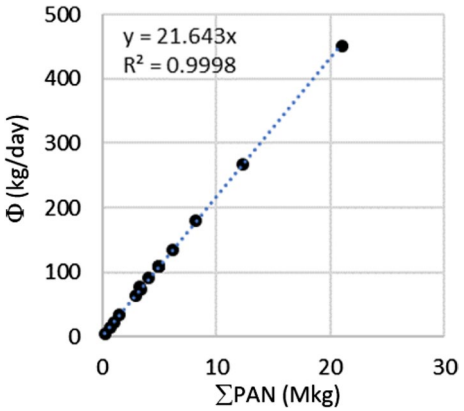

Fig. 15 Comparison between the amount of PAN created by the end of the wind-forcing period and the average phytoplankton production rate Φ (kg/day), derived from changes in total phytoplankton biomass during the second simulation week, for all experiments

trigger significant rates of $\Phi \approx 400$ kg/day. Our conceptual model is consistent with a linear relationship between Φ and D, but it does not explain why wind-driven nutrient upwelling does not develop for smaller islands (< 10 km in diameter). The explanation of this feature remains for future investigations.

Moreover, the predicted phytoplankton production rate Φ is also inversely proportional to the static stability of the pycnocline; that is, $\Phi \sim 1/M$ (Fig. 16d), which is also consistent with our conceptual model. Note that phytoplankton growth is largely suppressed for stability frequencies $M > 1/35$ s$^{-1} \approx 0.029$ s^{-1}. In this situation, the upwelling speed remains too low to lift nutrient-enriched water into the euphotic zone within the given time limit.

In summary, the phytoplankton production rate Φ increases with increasing wind stress (τ), prolonged duration of a wind event (t_w), and larger island diameter (D), and it decreases with a stronger static stability of the pycnocline (M), which is consistent with the conceptual model presented in Sect. 2.1. The functional relationship between these parameters can be written as follows:

$$\phi \sim \tau D M^{-1} t_w, \tag{12}$$

which is consistent with the model predictions (Fig. 17).

In addition to the functional relationships outlined above, we expect that Φ also depends on surface radiance (I_{oo}), mixed layer depth (h), the vertical nutrient gradient within the pycnocline, additional density effects due to presence of a barrier layer, and additional biological effects (e.g., zooplankton grazing), not considered in this study.

3.4 Final discussion

We show that, on a timescale of 14 days, short-lived wind events can create chlorophyll-*a* concentrations of ~ 0.2 mg/m^3 and vertical integrated values of ~ 10 mg/m^2 (see Fig. 13). The predicted values are of the order of magnitude of observational evidence by Gove et al. (2016) and Messié et al. (2022). Indeed, these values will continue to change over time under the effects of (i) gradual nutrient exhaustion or new nutrient enrichment from subsequent wind events, and (ii) zooplankton grazing (not considered here). Nevertheless, our findings confirm that wind-driven nutrient upwelling is a plausible mechanism behind the observed phytoplankton blooms.

Wind-driven upwelling around reef islands develops irrespective of the wind direction, which is different to the classical wind-driven coastal upwelling mechanism along continental margins (see Kämpf and Chapman 2016). Hence, it is possible that reef islands support wind-driven phytoplankton production throughout the year.

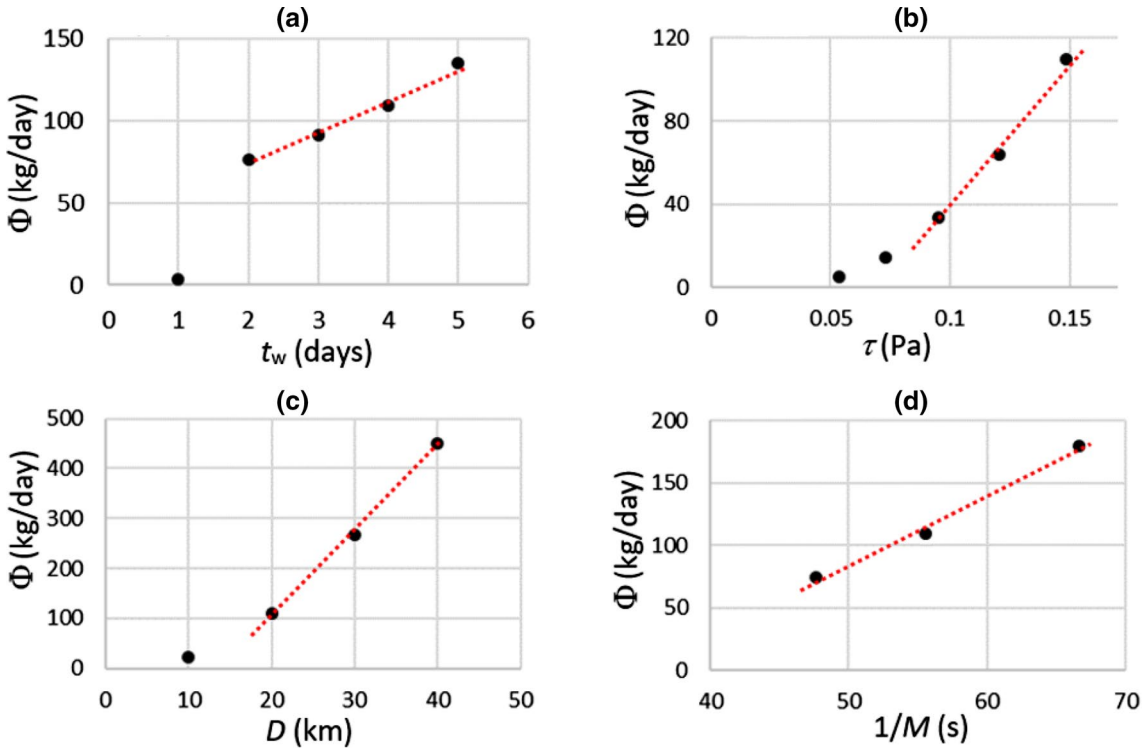

Fig. 16 Variation experiments (see Table 1). Average phytoplankton production rates, Φ (kg/day), as a function of **a** duration of wind events, t_w (days), **b** wind stress, τ (Pa), **c** diameter of the reef island, D (km), and the inverse of the stability frequency of the pycnocline, $1/N$ (s). Values of Φ are derived from changes in total phytoplankton biomass during the second simulation week. Dashed lines indicate linear trends

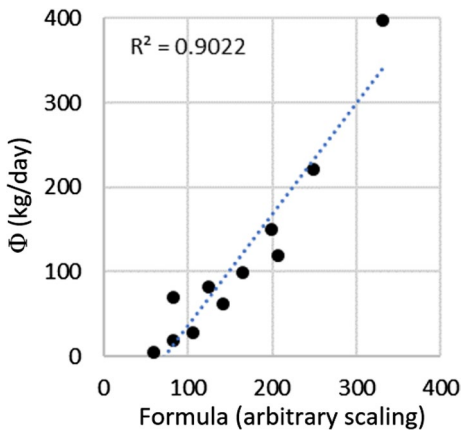

Fig. 17 Comparison of phytoplankton production rates Φ (kg/day) with values calculated from Eq. (12) for all experiments (see Table 1). The dashed line is the linear regression curve. Values of Φ are derived from changes in total phytoplankton biomass during the second simulation week

4 Conclusions

Using the method of process-oriented modelling, this study has enhanced the understanding of physical mechanisms inducing phytoplankton blooms in the oceans. There are several scientific questions that remain for future investigations. How does the wind-driven upwelling process interact with ambient geostrophic flows and island wakes? How do barrier layers influence the upwelling process? How do the topography of volcanic islands and the existence of shallow bathymetry around islands modify the upwelling process? Sea-level rise of 1–2 m on timescales > 100 years, further enhanced by wave erosion, will lead to the submergence of some barrier reefs (e.g., Bramante et al. 2020). Will this submergence decrease their ability to create phytoplankton blooms?

Acknowledgements This research has been supported by an internal research grant from the Marine and Coastal Research Consortium of the College of Science and Engineering, Flinders University. Wind data are data from Ifremer 6-hourly Long Time Series Satellite Surface Wind Analyses, available at http://apdrc.soest.hawaii.edu/data/data.php. Model codes used in this research are available from the corresponding author (jochen.kaempf@flinders.edu.au). Maps were produced with Scilab (https://www.scilab.org/), line graphs with Microsoft Excel.

Author contributions All authors contributed to the study conception and design. JK developed the computer models used in the study. All authors contributed to the analysis and interpretation of model results. In addition, AS and CC conducted comprehensive literature reviews of the island mass effect and ecological features associated with atoll reefs. The first draft of the manuscript was written by JK and all authors commented on previous versions of the manuscript. All authors read and approved the final manuscript.

Funding This research has been supported by an internal research grant from the Marine and Coastal Research Consortium of the College of Science and Engineering, Flinders University.

Data availability This work is purely theoretical and does not include new data collection. The model code used is available from the corresponding author.

Declarations

Conflict of interest None of the authors of this paper has financial or nonfinancial interests that are directly or indirectly related to the work submitted for publication.

References

Bell PRF (1992) Eutrophication and coral reefs—some examples in the Great Barrier Reef Lagoon. Water Res 26:553–568. https://doi.org/10.1016/0043-1354(92)90228-V

Blumberg AF, Mellor GL (2013) A description of a three-dimensional coastal ocean circulation model. In Heaps NS (ed) Three-Dimensional Coastal Ocean Models Coastal and Estuarine Sciences 4, AGU, https://doi.org/10.1029/CO004p0001

Bramante JF, Ashton AD, Storlazzi CD, Cheriton OM, Donnelly JP (2020) Sea level rise will drive divergent sediment transport patterns on fore reefs and reef flats, potentially causing erosion on atoll islands. J Geophys Res. https://doi.org/10.1029/2019JF005446

Caldeira RMA, Groom S, Miller P, Pilgrim D, Nezlin NP (2002) Sea-surface signatures of the island mass effect phenomena around Madeira Island. Northeast Atlantic Remote Sens Environ 80(2):336–360. https://doi.org/10.1016/S0034-4257(01)00316-9

Cronin MF, McPhaden MJ (2002) Barrier layer formation during westerly wind bursts. J Geophys Res 107(C12):8020. https://doi.org/10.1029/2001JC001171

Cushman-Roisin B, Beckers J-M (2011) Introduction to geophysical fluid dynamics: physical and numerical aspects, 2nd edn. Academic Press, p 796

Doty MS, Oguri M (1956) The island mass effect. J Cons Perm Int Explor Mer 22:33–37

Furnas MJ (1990) In situ growth rates of marine phytoplankton: approaches to measurement and species growth rates. J Plankton Res 12(6):1117–1151

Furuya K (1990) Subsurface chlorophyll maximum in the tropical and subtropical western Pacific Ocean: vertical profiles of phytoplankton biomass and its relationship with chlorophyll-a and particulate organic carbon. Mar Biol 107:529–539

Galperin B, Kantha LH, Hassid S, Rosati A (1988) A quasi-equilibrium turbulent energy model for geophysical flows. J Atm Sci 45:55–62

Goldberg WM (2016) Atolls of the world: revisiting the original checklist. Atoll Res Bull 610:1–47

Gove J, McManus M, Neuheimer A et al (2016) Near-island biological hotspots in barren ocean basins. Nat Commun 7:10581. https://doi.org/10.1038/ncomms10581

Griffin DA, Middleton JH, Bode L (1987) The tidal and longer-period circulation of Capricornia, southern Great Barrier Reef. Aust J Mar Freshw Res 38:461–474

Hanelt D (1992) Photoinhibition of photosynthesis in marine macrophytes of the South China Sea. Marine Ecol Prog Ser 82(2):199–206

Hasegawa D, Matsuno T, Tsutsumi E, Senjyu T, Endoh T, Tanaka T et al (2021) How a small reef in the Kuroshio cultivates the ocean. Geophys Res Lett. https://doi.org/10.1029/2020GL092063

Hwang DW, Kim G, Lee YW, Yang HS (2005) Estimating submarine inputs of groundwater and nutrients to a coastal bay using radium isotopes. Mar Chem 96(1):61–71

Jakobsen HH, Markager S (2016) Carbon-to-chlorophyll ratio for phytoplankton in temperate coastal waters: seasonal patterns and relationship to nutrients. Limnol Oceanogr 61:1853–1868. https://doi.org/10.1002/lno.10338

Ji R, Davis C, Chen C, Beardsley R (2007) Influence of local and external processes on the annual nitrogen cycle and primary productivity on Georges Bank: a 3-D biological–physical modeling study. J Mar Syst. https://doi.org/10.1016/j.jmarsys.2007.08.002

Kämpf J, Chapman P (2016) Upwelling system of the world. Springer Nature, Switzerland. https://doi.org/10.1007/978-3-319-42524-5

Kodaira T, Waseda T (2019) Tidally generated island wakes and surface water cooling over Izu Ridge. Ocean Dyn 69(11):1373–1385

Luyten PJ, Jones JE, Proctor R, Tabor A, Tett P, Wild-Allen K (1999) COHERENS - A Coupled Hydrodynamical-Ecological Model for Regional and Shelf Seas: User Documentation; MUMM Report; Management Unit of the North Sea: Brussels, Belgium, 914 pp., https://uol.de/f/5/inst/icbm/ag/physoz/download/from_emil/COHERENS/print/userguide.pdf. Accessed 1 May 2022

Mann KH, Lazier JRN (2005) Dynamics of marine ecosystems: biological-physical interactions in the oceans, 3rd edn. Blackwell Publishing, p 510

Mellor GL, Yamada T (1982) Development of a turbulence closure model for geophysical fluid problems. Rev Geophys Space Phy 20:851–875

Messié M, Petrenko A, Doglioli AM et al (2022) Basin-scale biogeochemical and ecological impacts of islands in the tropical Pacific Ocean. Nat Geosci 15:469–474. https://doi.org/10.1038/s41561-022-00957-8

Möller LM, Attard CRM, Bilgmann K et al (2020) Movements and behaviour of blue whales satellite tagged in an Australian upwelling system. Sci Rep 10:21165. https://doi.org/10.1038/s41598-020-78143-2

Nunn PD, Kumar L, Eliot I et al (2016) Classifying pacific islands. Geosci Lett 3:7. https://doi.org/10.1186/s40562-016-0041-8

Platt T, Gallegos CL, Harrison WG (1980) Photoinhibition of photosynthesis in natural assemblages of marine phytoplankton. J Mar Res 38:687–701

Schwartz ML, King CAM (2019) Lagoon. Encyclopedia Britannica, 23 Dec. 2019, https://www.britannica.com/science/lagoon-geography. Accessed 21 March 2022

Shchepetkin AF, McWilliams JC (2005) The regional oceanic modeling system (ROMS): a split-explicit, free-surface, topography-following-coordinate oceanic model. Ocean Modell 9(4):347–404. https://doi.org/10.1016/j.ocemod.2004.08.002

Smagorinsky J (1963) General circulation experiments with the primitive equations. I: the basic experiment. Mon Weather Rev 91:99–164. https://doi.org/10.1175/1520-0493(1963)091%3c0099:GCEWTP%3e2.3.CO;2

Spall MA, Pedlosky J (2013) Interaction of Ekman Layers and Islands. J Phys Oceanogr 43(5):1028–1041

Sprintall J, Tomczak M (1992) Evidence of the barrier layer in the surface layer of the tropics. J Geophys Res 97(C5):7305–7316. https://doi.org/10.1029/92JC00407

Street JH, Knee KL, Grossman EE, Paytan A (2008) Submarine groundwater discharge and nutrient addition to the coastal zone and coral reefs of leeward Hawai'i. Mar Chem 109:355–376

Vitousek PM, Mooney HA, Lubchenco J, Melillo JM (1997) Human domination of Earth's ecosystems. Science 277:494–499

Wu Q, Yu G, Ma Z, Ma S, Wu S (2016) Preliminary study on the fisheries catches in South China Sea via light falling-net fishing method. Int J Innov Stud Aquat Biol Fish (IJISABF) 2(5):1–4. https://doi.org/10.20431/2454-7670.0205001